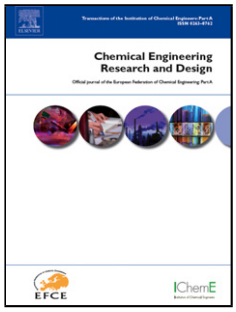

Title: Dynamic Characterization of Nanoparticles Production in a Droplet-based Continuous Flow Microreactor

Authors: Haiyun Ma, Nan Jin, Peng Zhang, Yufei Zhou, Yuchao Zhao, Xunli Zhang, Hongying L*ü*, Jie Liu

PII: S0263-8762(19)30053-X
DOI: https://doi.org/10.1016/j.cherd.2019.02.007
Reference: CHERD 3516

To appear in:

Received date: 1 November 2018
Revised date: 1 February 2019
Accepted date: 4 February 2019

Please cite this article as: Ma H, Jin N, Zhang P, Zhou Y, Zhao Y, Zhang X, L*ü* H, Liu J, Dynamic Characterization of Nanoparticles Production in a Droplet-based Continuous Flow Microreactor, *Chemical Engineering Research and Design* (2019), https://doi.org/10.1016/j.cherd.2019.02.007

Dynamic Characterization of Nanoparticles Production in a Droplet-based Continuous Flow Microreactor

Haiyun Ma[a,#], Nan Jin[a,#], Peng Zhang[a], Yufei Zhou[a], Yuchao Zhao[a,*], Xunli Zhang[b,*], Hongying Lü[a], Jie Liu[a]

[a]Shandong Collaborative Innovation Center of Light hydrocarbon transformation and utilization, College of Chemistry & Chemical Engineering, Yantai University, Yantai 264005, China

[b]School of Engineering & Institute for Life Sciences, University of Southampton, Southampton SO17 1BJ, UK

[*]Corresponding Authors.
E-mail address: yczhao@ytu.edu.cn (Yuchao Zhao), XL.Zhang@soton.ac.uk (Xunli Zhang).

[#]The authors contribute equally to the paper

GRAPHICAL ABSTACT

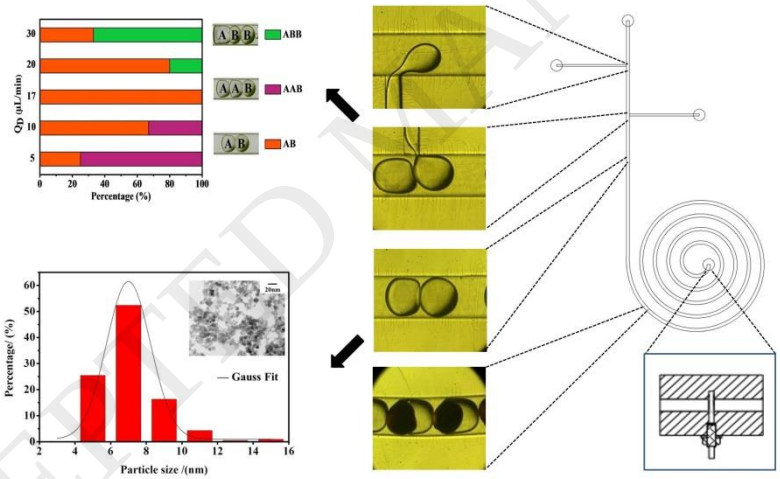

The highly dynamic process was characterised during iron oxide nanoparticles production within droplets under continuous flow in a spiral-shaped microreactor, which had a novel anti-clogging structure.

HIGHLIGHTS

- Highly dynamic process characterised during Fe_3O_4 nanoparticles production within droplets in a continuous flow microreactor
- A novel anti-clogging design incorporated into the microreactor for Fe_3O_4 nanoparticles synthesis
- One-to-one pairing and fusion of reactant droplets obtained under optimised flow conditions, at Q_D/Q_C = 0.3-0.5
- The break of liquid film between droplets after one-to-one pairing triggering the precipitation

Abstract

The present work was focused on the dynamic characterization of nanoparticles production under continuous flow in a droplet-based spiral-shaped microreactor. A novel drainage design was incorporated into the microreactor channel network for eliminating the commonly encountered problems of clogging and coalescence of microdroplets containing nanoparticles in the microchannel. Through precise manipulation of droplets formation for investigating the precipitation process of iron oxide, one-to-one pairing and fusion of reactant droplets were obtained and monitored in a real-time manner through digital imaging, where optimised flow rate ratios (in a range of 0.3-0.5) of aqueous phase to oil phase were applied. The nanoprecipitation process was observed and further analysed, indicating that the formation of precipitates was determined by the diffusion of OH^- after coalescence of reactants droplets. By characterising the Fe_3O_4 nanoparticles produced, it demonstrated that smaller droplets were beneficial to obtaining high quality nanoparticles in terms of size control and size distribution. Moreover, the kinetics of the nucleation process was investigated through statistic calculation. Initial results suggested that heterogeneous

nucleation occurring inside droplets was likely due to the presence of impurities-mediated (e.g. surfactants) or collision-induced nucleation events.

Keywords:
Microchannels; Droplets; Microreactors; Continuous-flow; Iron Oxide Nanoparticles

1. Introduction

The research and development of nanotechnology have been very active worldwide over the last decades, and nanomaterials have established their roles in many fields such as materials, electronics, engineering and life sciences (Laurent et al., 2008; Wu et al., 2008; Wahajuddin et al., 2012; Maleki et al., 2014; Zhong et al.,2006; Okoli et al., 2011; Jongnam et al., 2004; Leon et al., 2014). For the synthesis of nanomaterials, liquid-phase based methods have been widely applied in both laboratories and industries (Laurent et al., 2008; Wu et al., 2008; Jongnam et al., 2004), which mostly involved fast chemical reactions in the process of precipitation. In this process, high supersaturation was created in the local reaction area, resulting in nucleation mostly through a homogeneous nucleation mechanism, typically on a time scale of milliseconds (Davey et al., 2013; Dubrovskii et al., 2014). However, in the commonly-used stirring batch reactors the nucleation and crystallization took place in a complex multiscale hydrodynamic environment with inhomogeneity in both chemical and physical properties, e.g. the uneven distribution of chemical concentration and temperature, resulting in significant variation in reaction rate. That was largely attributed to the inhomogeneous mixing and caused difficulties for production in terms of controllability, reproducibility and quality assurance (Luis et al., 2014; Nguyen et al., 2016). Therefore, much research effort on the production of nanoparticles has been made to develop novel reactors capable of achieving effective mass transfer and mixing with high controllability (Jongnam et al., 2004; Erdem et al., 2013).

In the last decade, microreactors have been developed as useful research and manufacturing tools for a wide range of applications including nanoparticles synthesis

(Leon et al., 2014; Erdem et al., 2013; Lignos et al., 2017; Chan et al., 2003; Seemann et al., 2012; Gong et al., 2015). Compared with traditional batch-bulk processes, the flow and dispersion took place inside microreactor channels on the micro- to nano-scale. Not only have been found significant changes in reaction rate, conversion and selectivity on micro- or nano-scale, but also great improvements in heat transfer coefficient and mass transfer efficiency have been obtained (Leon et al., 2014; Erdem et al., 2013; Chan et al., 2003). Among a variety of microreactor configurations investigated, droplet-based microreactors have exhibited unique characteristics for nanoparticle synthesis, where a large number of monodispersed microdroplets acted as independent reactors which were surrounded and isolated by the continuous carrier phase (Erdem et al., 2013; Gong et al., 2015 Frenz et al., 2008). Compared with the single-phase continuous flow microreactors, droplet-based microreactors were able to enhance the mass transfer and realise rapid mixing due to the internal circulation within droplets (Song et al., 2003; Maeki et al., 2016; Ildefonso et al., 2012; Elviraet al., 2013; Basova et al., 2015; Wootton et al., 2012; Mashaghi et al., 2016; Mashaghi et al., 2016). In addition, the generated nanoparticles were wrapped in the droplets isolated by the carrier phase, which could effectively prevent nanomaterials from adhering to the microchannel wall and clogging the flow channel (Erdem et al., 2013; Frenz et al., 2008; Shum et al., 2010; Abou-Hassan et al., 2012; Wang et al., 2011; Vitry et al., 2015).

By using droplet-based microreactors, Liu et al. (2013) successfully synthesised nanoscale needle-shaped hydroxyapatite crystals having higher crystallinity, dispersibility, and aspect ratio than that obtained through conventional batch synthesis. By measuring the probability of crystal presence in the droplets as a function of time, Laval et al. (2009) characterised the nucleation kinetics of KNO_3 solution demonstrating that the nucleation followed a heterogeneous nucleation mechanism. For inducing coalescence and homogeneous nucleation across all droplets simultaneously, Luong et al. (2012) developed a thermocoalescence method to place microdroplets in a microfluidic chamber where droplets coalescence occurred at the same time when the system reached a critical temperature. In order to form and merge

droplets on-demand with high precision, Link et al. (2006) and Chabert et al. (2005) employed electrowetting techniques in combination with patterned electrodes embedded into the channel walls. In addition to the above mentioned methods, which rely on the external driving forces, specific geometry designs have been explored to passively optimise and control droplet generation and coalescence (Erdem et al., 2013; Hung et al., 2006; Deng et al., 2014). For example, Deng et al. (Deng et al., 2014) and Bremond et al. (Bremond et al., 2008) introduced an expanded chamber in the collection microchannel in order to reduce the local flow rates for assisting the droplets contact.

For the continuous flow synthesis of nanoparticles with microreactors, however, there still remain challenges to further improve the controllability and quality assurance of the nanoparticles produced with desired properties in terms of size and size distribution. This is largely due to the lack of insights into the highly dynamic process involving fluidics, mass transfer/mixing, and nanoprecipitation especially at the early stage, as well as the understanding of the nucleation kinetics (Song et al., 2003). In addition, within the microreactor flow channels large amounts of nanoparticles have been frequently found to block the microreactor outlet which was normally associated with micro-scale, complex geometries, posing a technical for operation.

Therefore, based on our previous studies (Zhao et al., 2006; Zhao et al., 2007), the aim of the present research was to further characterise the highly dynamic process of a droplet-based microfluidic reaction system in terms of droplet fluidics, morphology and coupled reactions. A model nanoprecipitation system was employed for the continuous synthesis of Fe_3O_4 nanoparticles, that have found a wide range of applications owing to their unique physiochemical e.g. magnetic properties. To successfully implement the process, a spiral-shaped droplet microreactor was developed by incorporating a novel drainage design in order to achieve anti-clogging and highly self-cleaning performance. Coupled with online imaging techniques, the microreactor system allowed us to characterise the dynamic process in a real time format for droplets formation, pairing, mixing and nanoprecipitation, and more

importantly, the interplays between these processes. Based on experimental observation, the nucleation kinetics was further analysed and the nucleation rate was estimated by calculating the nucleation frequency and the droplet volume within the microreactor. To evaluate the flexibility and universal application of the developed system, it has been extended to the synthesis of other nanomaterials.

2. Experimental

2.1 Materials

NaOH, $FeCl_3 \cdot 6H_2O$, $ZrOCl_2 \cdot 8H_2O$, $NH_3 \cdot H_2O$, $CaCl_2$, $NaCO_3$, $ZnCl_2$ were obtained from Sinopharm Chemical Reagent Company. $FeCl_2 \cdot 4H_2O$ was purchased from Tianjin BASF Chemical Company. n-Hexadecane and Span 80 were supplied by Tokyo Chemical Industry and Chengdu Kelong Chemical Reagent Company, respectively. Ethanol and acetone used for washing were produced by Sinopharm Chemical Reagent Company, and deionized water was produced in house. All the chemicals used were analytical reagent.

2.2 Microreactor system

The microfludic reactor was deigned in a sandwich structure consisting of a microchannel sheet (5 mm thickness) bonded between a top/cover plate and a bottom plate (both in a thickness of 10 mm). The microchannel was engraved by micromilling in a poly(methylmethacrylate) (PMMA) sheet, that was bonded to the top and bottom plates by thermal bonding at a temperature of 50 ^{o}C after washing in an ethanol bath of 70 ^{o}C.

Two opposite T-shaped junctions were designed to form three inlets, allowing one carrier phase to enter (via Inlet 1) the central main flow channel (500 μm × 500 μm, W × D), and two reactants flow (via Inlets 2 & 3) into the two side branch channels (150 μm × 150 μm, W × D) in a sequent format (Fig. 1(a)). The distance between the two T-junctions was 20 mm. In order to enhance the mixing process by the internal circulation flow in droplets, the main reaction channel was designed as a spiral shape. Three holes (Dia. 3.2 mm) were drilled through the top plate in order to connect the

supply pipes to the three inlet channels. In terms of operation, the microchannel network consisted of four functional sections; two T-junctions for droplets generation, a 70 mm-long straight main reaction microchannel for droplets pairing, and a 460 mm-long spiral microchannel for droplets fusion and nanoparticle formation.

Except for the spiral microchannel, a novel drainage structure was designed to prevent particles from the commonly encountered deposition and potential blockage near the outlet joint, as depicted in Fig. 1(b) and (c). Without this drainage structure, microchannel clogging can easily occur, as shown in Fig. S1(a) and (b) in the supporting information. The novel drainage structure consisted of three main parts, including the fluid buffer cavity, the flow channel connection, and the product outlet tubing. The buffering cavity (Φ1=1.8 mm) into the cover plate was fabricated, which was considered as a buffer pool for holding the continuous carrier phase. The depth of the buffering cavity (d4) was 5 mm, i.e., half of thickness of the top plate. The flow channel connection (Φ2=1.8 mm) through the middle sheet was designed to link the end of the microchannel and the aligned hole through the bottom plate. To match the different diameters of the buffering cavity (Φ1=1.8 mm), and the hole (Dia. 3.2 mm) through the bottom plate that was further linked to the external tubing with an external diameter (Φ4=3.2 mm) of 3.2 mm, the connection part in the drainage had two sections with corresponding diameters, i.e. 1.8 mm for the top section, and 3.2 mm for the bottom. During assembly it was crucial to ensure the bottom of the microchannel end to be on the same plane with the top of the inserted outlet tube (inner diameter Φ3=1.8 mm), in order to keep droplets flowing smoothly without deformation around the outlet joint, as shown in Fig. S1(c). A PTFE tube was used to help minimise potential particle deposition on the tube wall surface.

2.3 Synthesis of Fe_3O_4 nanoparticles with microreactor

Through Inlet 1 (Fig. 1), n-hexadecane serving as the carrier phase was injected into the central main microchannel with syringe pump (LSP01-1BH, Baoding Longer Precision Pump Company) at a flow rate of 20-150 μL/min. NaOH solution (via Inlet 2) and $FeCl_2$/$FeCl_3$ mixture solution (via Inlet 3) were introduced into the two

T-junctions as the dispersed phases at a given equal flow rate, i.e. with a volumetric flow rate ratio of 1:1. After dispersing the droplets in the oil phase, the aqueous droplets in sequence underwent pairing and fusion, allowing Fe_3O_4 nanoparticles generated within the merged and mixed droplets along the main flow channel.

Based on the analysis of the chemical processes (see the Supplementary Material, SM), the concentration ratio of $Fe^{2+}/Fe^{3+}/OH^-$ was set as 1:2:16 in this work. The concentration of NaOH solution was 1.92 mol/L, and that of $FeCl_2/FeCl_3$ solution was 0.12 mol/L and 0.24 mol/L for Fe^{2+} and Fe^{3+}, respectively. To prevent Fe_3O_4 from being further oxidized into Fe_2O_3, all the aforementioned solutions were purged with nitrogen about 10 mins for eliminating oxygen.

To obtain stable droplets, Span 80 was added into the continuous carrier phase at a concentration of 10 wt%. The flow rates of the two aqueous solutions were set to be equal so that the droplets were paired one-to-one. At the outlet, the droplets and the carrier phase were collected in the vials at room temperature. Following centrifugation (15777 G), the solid product was washed three times with acetone, water/ethanol/acetone (1:1:1, vol/vol), respectively, to remove the impurities, such as n-hexadecane, Span 80, Cl^-, residual Fe^{2+}, Fe^{3+}, and OH^-. The washed precipitates were then dried by frozen dryer as the final product.

2.4 Imaging dynamic processes of flow and reaction

An inverted microscope (Olympus IX73), a stereo microscope (Olympus SZX16,) and a high-speed digital camera (Phantom R311) were employed for imaging and recording the flow, droplet behaviour and reaction processes at a speed of 3200 frames per second, and subsequently processed by the image analysis program (Image J). At least three runs were repeated in each selected area of interest along the main reaction channel.

2.5 Characterization of nanoparticles

The produced nanoparticles were characterized by X-ray diffraction (XRD) and transmission electron microscope (TEM). The crystalline phases of the samples were examined by XRD analysis (XRD-6000, Shimadzu, Japan), using Cu Kα radiation (λ

= 0.15406 nm) in the 2θ range of 20° to 80° at a scan rate of 10°/min. Spectrum analysis software, MDI Jade V6.0, was used to identify the crystallographic phase composition. The morphology and structure of Fe_3O_4 particles were characterised by TEM (JEM-2000 EX). The size and its distribution of the Fe_3O_4 nanoparticles obtained were determined by averaging the sizes of 200 particles from TEM images.

2.6 Calculation of nucleation kinetics

The analysis of nucleation kinetics was based on counting the number of empty droplets as a function of time and assuming that the nucleation process can be described by a Poisson process (Vitry et al., 2015). Due to that the droplets generated in the microchannel are small enough the time required for the nucleation is much larger than the time for the nucleus growth, and so only nucleation is assumed to occur. In this case, nucleation is a stochastic process, which can be expressed by Eq. 1. The nucleation rate J, the number of nuclei produced by unit of time and volume, can be calculated by Eq. 2 (Laval et al., 2009; Goh et al., 2010).

$$P(t) = 1 - \exp(-\omega t) \quad (1)$$

$$J = \omega / V \quad (2)$$

where ω is the nucleation frequency, i.e. the nuclei number formed per unit time. V is the droplet volume, and P(t) is the non-dimensional probability that a droplet does contain crystals.

To calculate the nucleation probability, the droplets number was collected from over twenty locations in each run (Fig. S1 in the SM). The position at the inlet of spiral zone was assumed as initial time (t=0). The spiral microchannel was divided into eight zones, and there were about 10-20 droplets in each zone. By the microscope and the high-speed camera, the real-time images were recorded along the spiral microchannel. Through counting the droplets containing visible crystals, the probability P was determined. The probability P was only determined by the number of droplets where the crystals existed, and independent of shape and state of crystals. All experiments were repeated ten times at least and averaged the results for eliminating any possible discrepancies.

As shown in Eq. 1, [1-P(t)] was expected to follow an exponential decay characterized by the nucleation frequency. The nucleation frequency under different conditions could be estimated by fitting the experimental data. The hydrodynamic characteristics of droplets in the oil phase remained constant, and so the droplets volume was mainly controlled by the flow rates and measured by $V=V_{OH^-}+V_{Fe^{2+}/Fe^{3+}}$, where V_{OH^-} and $V_{Fe^{2+}/Fe^{3+}}$ refer to the droplets volume of OH^- and Fe^{2+}/Fe^{3+} solution, respectively. Finally, the nucleation rate could be estimated by calculating the nucleation frequency and the droplet volume.

3. Results and discussion

3.1 General observation of droplets behaviour

During the generation and flow of droplets along the microfluidic reaction channel, four stages were observed, (a) droplets dispersion, (b) droplets collision, (c) droplets pairing, and (d) droplets fusion where reaction took place for Fe_3O_4 nanoparticles formation, as shown in Fig. 2.

The droplets of NaOH and Fe^{2+}/Fe^{3+} were generated at the first and second T-junction, respectively. At the droplets generation stage, the Fe^{2+}/Fe^{3+} droplet "met" at the second T-junction until the arriving of the NaOH droplet, and a pair of droplets was formed. It was observed NaOH and Fe^{2+}/Fe^{3+} droplet pairs were steadily dispersed in the continuous carrier phase and flowing along the straight main microchannel. After entering into the spiral microchannel section, paired droplets began to fuse, while triggered the nucleation-crystallization process for Fe_3O_4 nanoparticles formation. The aforementioned four stages are further analysed in detail, as follows.

3.2 Droplets generation

In order to understand and control the droplet generation, the droplet formation process of Fe^{2+}/Fe^{3+} and NaOH phases in the carrier phase were investigated in a range of 5-40 μL/min for the dispersed phases (Q_D), with a given flow rate of 40

μL/min for the carrier phase (Q_C). The effects of the dispersed phase flow rate on the droplets formation were illustrated in Fig. 3.

Three kinds of flow patterns were observed for the OH^- phase under these operating conditions, that is, dripping, jetting, and none break-up flow as shown in Fig. 3. The formation of dispersed droplets in microchannels was governed mainly by the competition between the driving forces (shear force exerted on the droplet phase by continuous phase, interfacial tension at the interface of two phases) and the resistance forces (viscous force, inertial force of dispersed phase) (Ushikubo et al., 2014; Wang et al., 2013; Wang et al., 2009), all of which could be affected by Q_C and Q_D. At a given Q_C, an increase in Q_D could increase the pressure of the dispersed phase, which resulted in the transition from the dripping to the jetting flow. When the effects of viscous force were significantly larger than the interfacial force, the formation of droplet was impeded, where none break-up flow took place.

In contrast to the OH^- phase, only two kinds of flow patterns were observed for the Fe^{2+}/Fe^{3+} phase, where the dripping flow existed in the range of 5-20 μL/min for Q_D, and then converted into none break-up flow as Q_D increase to 40 μL/min. This was largely attributed to the differences in the interfacial tensions between n-hexadecane-$FeCl_2/FeCl_3$ (5.62 mN/m) and n-hexadecane-NaOH phases (0.39 mN/m). As could be seen from our experiments, the shape of Fe^{2+}/Fe^{3+} droplets kept approximately spherical under all operating flow conditions, while that of OH^- droplets appeared to be more irregular. These phenomena also indicated that the interfacial force between $FeCl_2/FeCl_3$ and n-hexadecane phases was stronger than NaOH phases. As a result, the $FeCl_2/FeCl_3$ phase was easier to form droplets in the n-hexadecane carrier phase than NaOH phase, as observed in the range of 10-20 μL/min for Q_D.

Table 1 provided Capillary numbers (Ca) under the corresponding conditions, which could further distinguish the droplet formation regimes. On the whole，Capillary numbers of Fe^{2+}/Fe^{3+} droplets were less than that of OH^- droplets with one order of magnitude, which were also consistent with the experimental results that the

$FeCl_2$/$FeCl_3$ droplets was easier to form the dripping. In our experiments, the critical Ca values to distinguish dripping, jetting and none break-up were about 10^{-3} and 5×10^{-3}, which were consistent with other literatures (Wu et al., 2017; Yagodnitsyna et al., 2016). But remarkably, the transition from jetting to none break-up for OH^- droplet was strongly dependent on the distance between two T-junctions. This was explained the Fe^{2+}/Fe^{3+} droplet formed at the T-junction-2 limited the extension of flow thread, which could mix two aqueous s directly, as shown in Fig. 3(e)&(j).

3.3 Droplets collision and pairing

After the formation of dispersed droplets, Fe^{2+}/Fe^{3+} and OH^- droplets underwent collision and pairing at the second T-junction, where the pairing mode could directly determine the efficiency and homogeneity of crystallisation. The creation of different pairing modes was examined for Q_D in the range of 5-30 μL/min at a given continuous phase flow rate of 40 μL/min, as shown in Fig. 4.

As could be seen in Fig. 4, three kinds of aqueous droplet pairing modes were observed, namely, AAB (i.e. OH^--OH^--Fe^{2+}/Fe^{3+}), ABB (i.e. OH^--Fe^{2+}/Fe^{3+}-Fe^{2+}/Fe^{3+}) and AB (i.e. OH^--Fe^{2+}/Fe^{3+}). When Q_D was lower than the half of Q_C and set at 5 or 10 μL/min, AAB mode appeared and accounted for 75% and 33%, respectively. When Q_D was equal to the half of Q_C, AAB mode disappeared and ABB mode appeared with proportion of 20%. Moreover, the alternately ranged AB mode was created under all operating conditions. By increasing Q_D, the proportion of AB mode increased and reached 100% for Q_D =17 μL/min, and then decreased, where existed an optimal operating condition. Further increasing Q_D to 30 μL/min, ABB became to a dominant mode. AB mode was an ideal mode according to the reaction stoichiometry, that is "one-to-one" mode, where droplet pairing showed high reaction efficiency (Frenz et al., 2008; Liu et al., 2013). It was also seen from Fig. 4 that the AB mode could be created under all operating conditions, however, the higher flow rate induced an unstable flow, e.g. forming small droplets (Fig. 5). And the optimal Q_D/Q_C ratio was

found to be 0.3-0.5 for AB mode droplet pairing under the operational conditions.

The formation of ABB, AB and AAB pairing patterns were attributed to the different formation frequency of two droplets, which caused by the different physical properties of OH^- and Fe^{2+}/Fe^{3+} phases. When Q_D was low, both two droplets formed by the dripping. Compared with the formation of OH^- droplet at the T-junction-1, the Fe^{2+}/Fe^{3+} droplet at T-junction-2 was more complex due to the additional impact from the dispersed phase in the front branch channel. Moreover, the pressure build-up of the dispersed phase was slow due to the larger outlet pressure of the T-junction-2. The generation rate of Fe^{2+}/Fe^{3+} droplet was smaller in comparison with OH^- droplet, which induced the AAB mode of droplet pairing. With increasing of Q_D, the Fe^{2+}/Fe^{3+} droplet still formed by the dripping, which resulted in little changes in the droplet size and formation frequency due to the interfacial tension. Whereas the OH^- droplet formation mechanism transformed from the dripping into the jetting, in which the droplet formation was dominated by the interfacial tension and the viscosity force. The viscosity force increased with Q_D, which led to more time for continuous phase to pinch off the OH^- droplet. Hence, the frequency of OH^- droplet formation gradually decreased and the ABB pairing mode appeared. In addition, the AAB and ABB pairing modes did not occur together. To make the balance of same flow rate of OH^- and Fe^{2+}/Fe^{3+} phases, the average volume of Fe^{2+}/Fe^{3+} droplet was larger than that of OH^- droplet in AAB mode, whereas the average volume of OH^- droplet was larger than that of Fe^{2+}/Fe^{3+} droplet for ABB mode.

To further explore the operational window of AB mode, Q_C varied in the range of 40-150 μL/min in combination with specific Q_D that matched Q_C, as shown in Fig. 5. The dispersed droplets of OH^- phase were mainly formed by the jetting flow, as shown in Fig. 3. Both Q_C and Q_D increased simultaneously, the fluid thread of OH^- phase originated from the first T-junction was lengthened and even extended to the second T-junction, this could be seen from Fig. 5. In that case the formation of Fe^{2+}/Fe^{3+} phase droplets was driven by the extended OH^- phase fluid thread, as well as their shapes and sizes. Therefore, the distance between two junctions was enough long

to provide appropriate travel time for forming independent dispersed droplets at the second junction, especially at high flow rates.

3.4 Droplets fusion and nanoparticles formation

Under the optimised operational conditions, following droplets generation, collision and pairing they flowed along the main reaction channel in a steady and stable way to undergo fusion while nanoprecipitation started to take place. In principle, the droplets fusion process involves a series of dynamic stages across their interface, including interface consumption, interface fusion, permeation and encapsulation. The dynamic changes across the interface between droplets were examined in detail by following a pair of droplets along the flow channel. Fig. 6 shows example images at different stages of fusion, captured at Q_C and Q_D of 20 µL/min and 8 µL/min, respectively.

Initially, the generated droplets containing OH^- and Fe^{2+}/Fe^{3+} phases contacted with each other, and the liquid film between the two droplets disappeared (Fig. 6a-d). Then, the solute near the film erupted gradually from the solution into a nucleus, and subsequently unreacted OH^- reacted with Fe^{2+}/Fe^{3+} through internal circulation and diffusion (Fig. 6e&f). Finally, the droplets further merged, and the precipitates formed within the droplets (Fig. 6g&h).

During the formation of Fe_3O_4, it was observed that when the droplets containing OH^- and Fe^{2+}/Fe^{3+} phases merged, precipitation occurred almost simultaneously on the contact site, starting at the centre of the microchannel, resulting in a precipitation film. It was also noticed that the precipitation film appeared to be curved (Fig. 6e), where the ruptured droplet film became invisible. This was likely due to the fact that the liquid film of OH^- phase broke up prior to that of Fe^{2+}/Fe^{3+} phase. Unlike the elastic droplets film, the liquid film recessing into another droplet surface cannot be recovered, hence the right side of the merged droplets remained the original shape of the Fe^{2+}/Fe^{3+} droplets (Fig. 6g&h).

It was also observed (Fig. 6g-h) that the precipitation took place quickly (about 4 millisecond) within the fusion space, where the Fe^{2+}/Fe^{3+} phase originally, towards a

uniform state. This clearly indicated that the precipitation process was a result of diffusion of OH^- through the intermediate film into Fe^{2+}/Fe^{3+} phase. This was explained the diffusion coefficient of OH^- ion was intensively larger than Fe^{2+}/Fe^{3+} in aqueous solution (Cussler et al., 2009). In addition, the enhanced mixing by internal circulation in the droplets contributed further to eliminating the concentration gradient of OH^- and Fe^{2+}/Fe^{3+}, as demonstrated in previous study (Liu et al., 2013). This quickly achieved homogeneity was beneficial for creating uniformity of crystal nucleus size and ultimately, the nanoparticles' geometry.

In this regard, the adoption of spiral-shaped microchannel further accelerated the mixing process. Specifically, the existence of centripetal force increased the frictional force in the spiral structure compared with that in the straight microchannel, leading to the negative velocity gradient of continuous phase. Consequently, the resistance of droplets increased and the droplets slowed down as they flowed through this zone. With the change of the curvature of the curved channel, the two droplets kept getting close, and subsequently broke up and fused for mixing and reaction, as shown in Fig. 6c-h. Furthermore, during the precipitation process, the reaction between Fe^{2+}/Fe^{3+} and OH^- was confined into a limited reaction chamber, in which the content of Fe^{2+}/Fe^{3+} was limited. Therefore, generated Fe_3O_4 NPs from different reaction cells had uniform quantity. As the obtained Fe_3O_4 NPs were entrapped in the reaction cell, which was isolated by oil, this configuration helped further prevent Fe_3O_4 nanoparticles from oxidised to Fe_2O_3.

Moreover, by incorporating the novel flow outlet drainage, the reactor system could be successfully operated in a continuous way for up to 48 hours without clogging either on the channel wall or at the outlet. The yield of precipitates remained above 94%.

3.5 Characterization of iron oxide nanoparticles

TEM analysis (Fig. 7 & Fig. S2) confirmed the size and size distribution of the nanoparticles produced under different flow conditions. At lower flow rates (i.e. 40 and 80 μL/min), the longer residence time allowed for the further progression of

crystallization inside droplets, where the average particle size was about 7 nm. In contrast, at higher flow rates (i.e. 120 and 150 μL/min), the residence time within the reaction channel was shorter that the time required for reaction completion, giving an average size of 4-6 nm. In this case, the crystallization process may proceed even after leaving the microreactor, leading to uncontrolled mixing and hence the formation of larger (up to 20 nm) and non-uniform nanoparticles with a wider size distribution. In addition, the content of small particles increased with the increase of the two phase flow velocity, but the particle size distribution broadened at the high flow rate due to collision caused by flow turbulence.

Table 2 summarises the crystallinities of the iron oxide nanoparticles produced under different flow conditions based on the XRD analysis (Fig. S3). The results showed relatively low crystallinities ranging from 22.07% to 38.86% for the Fe_3O_4 nanoparticles, this might be associated with the relatively low reaction temperature, i.e. room temperature about 20 ^oC. The results confirmed that the microreactor system was capable of producing Fe_3O_4 nanoparticles with monodispersity effectively, as optimal operational flow conditions were able to reduce the possibility of nanoparticle coalescence.

On the whole, the experimental results were in good agreement with many literatures (Frenz et al., 2008; Phillips et al., 2014; Abou-Hassan et al., 2008). The nanoparticle size was comparable with the results of Frenz et.al. and Abou-Hassan et.al., who synthesized iron oxide NPs in different microreactors with the size of 4 nm and 7 nm, respectively (Frenz et al., 2008; Abou-Hassan et al., 2008). In addition, the dispersity, morphology and crystallinity of iron oxide nanoparticles synthesized by this system were better than previous studies through the comparison of TEM image with the result of Simmons et.al. (Fig. S5)

3.6 Determination of nucleation kinetics

As generally understood, the primary nucleation induction period in crystallization consisted of the time required for the nucleation and the growth time of the nucleus to the detectable dimension (Ildefonso et al., 2012; Vitry et al., 2015; Laval et al., 2009). However, it was normally difficult to detect and quantify this process. In this regard, the development of methodologies for the characterisation of the dynamic processes of flow and reaction by visualisation through digital imaging droplets along the microfluidic channel provided useful tools for the determination of nucleation process. Besides, in the droplets method, it was necessary to verify that the presence of crystals in the one droplet did not affect the nucleation in others, for example, due to contamination and clogging of microchannels. Therefore, the design and functionality of novel mircoreactors were also tested on the basis of the determination of nucleation process. Based on the analysis of some droplets at each position in the microchannel(Vitry et al., 2015), P(t), the non-dimensional probability of a droplet containing crystals, was determined by analysing the images captured at selected positions and time points.

Fig. 8 presented the temporal evolution of P at Q_C = 40-150 μL/min with corresponding Q_D = 17-45 μL/min. Time 0 was set at the inlet of the spiral channel. In the initial period, paired droplets entered into the spiral channel before fusion and reaction, the nucleation probability was 0, hence this period was named as the delay period. After the droplets containing reaction solutions with an enough supersaturation merged, the first nuclei generated and the merged droplets entered into the nucleation, in which P constantly increased with time.

To be clear, the delay period in Fig. 8 referred to the time for generating the first nuclei, which was related to the breakup time of liquid film between OH^- and Fe^{2+}/Fe^{3+} droplets. When all droplets were nucleated, it could be considered that nucleation was finished and P was up to 1. Within the scope of the investigated flow rates, almost all droplets completed nucleation before leaving the microreactor. However, when Q_C and Q_D increased to 150 and 45 μL/min, respectively, the

residence time was limited by the length of microreactor and the measured maximum nucleation probability was 0.92. This suggested a range of residence times be appropriate for plausible nucleation in a given reactor.

With the increase of Q_C, the delay time increased from 0 s to 17 s, as shown in Fig. 8. Fusion of paired droplets was mainly driven by the interfacial tension, and inhibited by viscous force and inertial force. As analyzed above, the special spiral structure reduced the droplets velocity along the channel, as well as the inertia force and viscous force. As the total flow rate increased, the inertial force and viscous force increased, making droplets fusion difficult. Therefore, the stress transition required for the droplets breaking was improved, and correspondingly the channel structural curvature should be increased to reduce inertial force and viscous force, that is, the induction time grew longer. However, the increase of flow rate would also increase the degree of fluid circulation both inside and outside. Therefore, the time required to complete the nucleation of all droplets was slightly reduced.

The relationship between ln(1-P) and time was further plotted in Fig. 9, together with fitting line. As expressed in Eqs. 1 & 2, ln(1-P) versus time was expected to fit into a linear relationship with a slope of ω and intercept of 0. However, the results displayed in Fig. 9 could not be accounted by simple linear behaviours but rather by $ln(1-P) = -\omega t + \varepsilon$. It was interesting to note that, in the range of the errors permitted, the value of (1-P) decreased exponentially with time. This was most likely associated with the presence of impurities-mediated (e.g. surfactant) or collision-induced nucleation events, though this needed further confirmation (Vitry et al., 2015). When the crystallization occurred, the inclusion or other solid phase surface inside the droplets would be used as the substrate to form the nuclei, and the surface energy required for the crystallization process would be much smaller than that required for automatic nucleation. Except for impurities, in the case of diffusion-controlled mixing and nucleation process, the rapid heterogeneous nucleation could be also induced with an increase in flow rate which enhanced the mixing performance.

Based on the fitting lines, ω values at different flow rates were obtained and listed in Table 3. The average volume of fused droplets and the nucleation rates J were then calculated roughly and also included in the Table. Results showed that the nucleation rate J increased with flow rate at first and then decreased as flow rate continued to increase. This could be attributed to the combined influence of the droplet volume and internal circulation. With the increase of flow rate, the droplet volume changed inversely (as listed in Table 3), making the nucleation rate decrease due to the stochasticity of the process. Meanwhile, the internal circulation inside the droplet was intensified at high flow rate, so did the nucleation rate. When the flow rate was less than 200 μL/min, the influence of internal circulation on the nucleation rate was greater than that of the droplet volume, which led to the intensification of the nucleation process. When the flow rate reached 240 μL/min, small changes in the intensity of the internal circulation made the droplet volume the dominant factor, which slowed down the nucleation process. In addition, there was no uniform variable due to the non-uniqueness of pairing ratio at different flow rate, and a series of detailed studies on the nucleation rate would be conducted in the future work.

3.7 Universal application of this system

Having developed an easy-to-use anti-clogging system, we then explored the flexibility and universal application of this developed system through the precipitation process of $CaCO_3$, ZrO_2 and ZnO nanoparticles. As shown in Fig. 10, the precipitation process of $CaCO_3$, similar to synthesis process of Fe_3O_4, was conducted by merging the Ca^{2+}-containing droplet with the CO_3^{2-}-containing one. The merged droplet served as a reaction cell, and, as a result, the synthesis reaction occurred in a confined space, which not only the fast reaction controllable, but avoided the deposition of solid product on the microchannel walls.

The device was then used to prepare zirconia and zinc oxide nanoparticles within droplets, all of which verified the applicability of the device on precipitation reaction

and nanoparticle synthesis. In each case, consecutive run with more than 48 hours was conducted in the microreactor without adsorption of nanoparticles on the microchannel walls and at the outlets. After one run of the microreactor, more than 94% product was obtained, with a few loss attributed to particle adsorption during the separation procedures. The XRD patterns of the ZrO_2 and ZnO nanoparticles are shown in Fig. S5 and S6, based on which the average diameters of these particles were calculated with about 8 nm. In summary, the careful control of precipitation gave nanoparticles of uniform size and good dispersion in the microreactor while avoiding channel blockage, and no fouling observed after multiple time of operation.

4. Conclusions

With a droplet-based spiral-shaped microreactor, the highly dynamic process was characterised during iron oxide nanoparticles production within droplets under continuous flow. A novel drainage design was incorporated into the microreactor channel network which successfully eliminated the commonly encountered problems of clogging and coalescence of microdroplets containing nanoparticles in the microchannel. The experimental results revealed the optimised flow rate of aqueous phases, at a given carrier phase flor rate, facilitated the fully creation of the desired one-to-one drops pairing, where the two-phase flow ratio (Q_D/Q_C) was 0.3-0.5. The droplet-based nanoprecipitation process was investigated through visualisation, showing that the nanoparticles formation process involved a chain process, including droplets collision, interface consumption, interface fusion, permeation and encapsulation. It was also found that the formation of precipitates was determined by the diffusion of OH^- after coalescence of reactants droplets. By characterising the Fe_3O_4 nanoparticles produced, it demonstrated that smaller droplets was beneficial to obtaining high quality nanoparticles in terms of size control and size distribution. Based on this, precipitation process of $CaCO_3$ was observed and synthesis of ZrO_2, ZnO nanoparticles were also conducted, all of which verified the flexibility and universal application of the developed system. Moreover, the kinetics of the nucleation process was analysed by calculating the nucleation rate. Initial results suggested residence times be appropriate for plausible nucleation in a given reactor. And heterogeneous nucleation occurring inside droplets was likely due to the presence of impurities-mediated (e.g. surfactants) or collision-induced nucleation events. In order to further elucidate the mechanism of such complex nucleation process involving many influencing factors, further investigation is needed, which is ongoing in our laboratories.

Acknowledgments

We gratefully acknowledge the financial supports from National Natural Science Foundation of China (Nos. 21808194, 21676230), State Key Laboratory of Chemical Engineering (SKL-ChE-17A04), Shandong Provincial Natural Science Foundation (ZR2017BB058) and China Shipbuilding Industry Corporation United Foundation (6141B04080206).

References

Abou-Hassan, A., Neven, S., Dupuis, V., Cabuil, V., 2012. Synthesis of cobalt ferrite nanoparticles in continuous-flow microreactors. RSC. Adv. 2, 11263-11266.

Abou Hassan, A., Sandre, O., Cabuil, V., Tabeling, P., 2008. Synthesis of goethite by separation of the nucleation and growth processes of ferrihydrite nanoparticles using microfliudics. Angew. Chem. Int. Ed. 1783-1785.

Basova, E.Y., Foret, F., 2015. Droplet microfluidics in (bio) chemical analysis. Anal. Sci. 140, 22-38.

Bremond, N., Thiam, A.R., Bibette, J., 2008. Decompressing emulsion droplets favors coalescence. Phys. Rev. Lett. 100, 024501.

Chan, E.M., Mathies, R.A., Alivisatos, A.P., 2003. Size-controlled growth of CdSe nanocrystals in microfluidic reactors. Nano Lett. 3, 199-201.

Chabert. M., Dorfman, K.D., Viovy, J.L., 2005. Droplet fusion by alternating current (AC) field electrocoalescence in microchannels. Electrophoresis. 26, 3706-3715.

Cussler, E.L., 2009. Diffusion mass transfer in fluid systems. Cambridge University Press.

Davey, R.J., Schroeder, S.L.M., ter Horst, J.H., 2013. Nucleation of organic crystals - a molecular perspective. Angew. Chem. Int. Ed. 52, 2166-2179.

Dubrovskii, V.G., 2014. Nucleation theory and growth of nanostructures. Springer. Berlin.

Deng, N.N., Sun, J., Wang, W., Ju, X.J., Xie, R., Chu, L.Y., 2014. Wetting-induced coalescence of nanoliter drops as microreactors in microfluidics. ACS Appl. Mater. Inter. 6, 3817-3821.

De Menech, M., Garstecki, P., Jousse, F., Stone, H.A., 2008. Transition from squeezing to dripping in a microfluidic T-shaped junction. J. Fluid Mech. 595, 141-161.

Erdem, E.Y., 2013. Microfluidic reactors for the controlled synthesis of monodisperse nanoparticles. University of California. Berkeley.

Elvira, K.S., Solvas, X.C., Wootton, R.C.R., 2013. The past, present and potential for microfluidic reactor technology in chemical synthesis. Nature Chem. 5, 905-915.

Frenz, L., El Harrak, A., Pauly, M., Begin-Colin, S., Griffiths, A.D., Baret, J.C., 2008. Droplet-based microreactors for the synthesis of magnetic iron oxide nanoparticles. Angew. Chem. Int. Ed. 47, 6817-6820.

Gong, X.Q., Wang, Y.W., Ihli, J., Kim, Y.Y., Li, S.B., Walshaw, R., Li, C., 2015. The crystal hotel: a microfluidic approach to biomimetic crystallization. Adv. Mater. 27, 7395-7400.

Goh, L., Chen, K., Bhamidi, V., He. G.W., Kee, N.C.S., Kenis, P.J.A., Zukoski, C.F., Braatz, R.D., 2010. A stochastic model for nucleation kinetics determination in droplet-based microfluidic systems. Cryst. Growth. Des. 10, 2515-2521.

Hung, L.H., Choi, K.M., Tseng, W.Y., Tan, Y.C., Shea, K.J., Lee, A.P., 2006. Alternating droplet generation and controlled dynamic droplet fusion in microfluidic device for CdS nanoparticle synthesis. Lab on a Chip. 6, 174-178.

Ildefonso, M., Revalor, E., Punniam, P., Salmon, J.B., Candoni, N., Veesler, S., 2012. Nucleation and polymorphism explored via an easy-to-use microfluidic tool. J. Cryst. Growth. 342, 9-12.

Jongnam, P., Kwangjin, A., Yosun, H., Je-Geun, P., Han-Jin, N., Jae-Young, K., Jae-Hoon, P., Nong-Moon, H., Taeghwan, H., 2004. Ultra-large-scale syntheses of monodisperse nanocrystals. Nature Mater. 3, 891-895.

Laurent, S., Forge, D., Port, M., Roch, A., Robic, C., Vander, E.L., Muller, R.N., 2008. Magnetic iron oxide nanoparticles: synthesis, stabilization, vectorization, physicochemical characterizations, and biological applications. Chem. Rev. 108, 2064-2110.

Laval, P., Aurore, C., Salmon, J.B., 2009. Microfluidic droplet method for ncleation kinetics measurements. Langmuir. 25, 1836-1841.

Leon, R.A.L., Wan, W.Y., Badruddoza, A.Z.M., Hatton, T.A., Khan, S.A., 2014. Simultaneous spherical crystallization and co-formulation of drug(s) and excipient from microfluidic double emulsions. Cryst. Growth Des. 14, 140-146.

Lignos, I., Maceiczyk, R., Demello, A.J., 2017. Microfluidic technology: uncovering

the mechanisms of nanocrystal nucleation and growth. Acc. Chem. Res. 50, 1248-1257.

Link, D.R., Grasland-Mongrain, E., Duri, A., Sarrazin, F., Cheng, Z.D., Cristobal, G., Marquez, M., Weitz, D.A., 2006. Electric control of droplets in microfluidic devices. Angew. Chem. Int. Ed. 118, 2618-2622.

Liu, K.Y., Qin J.H., 2013. Droplet-fused microreactors for room temperature synthesis of nanoscale needle-like hydroxyapatite. Nanotechnology. 24, 125602-125609.

Luis, P.J., 2014. Microfluidic platforms: a mainstream technology for the preparation of crystals. Chem. Soc. Rev. 43, 2253-2271.

Luong, T.D., Nguyen, N.T., Sposito, A., 2012. Thermocoalescence of microdroplets in a microfluidic chamber. Appl. Phys. Lett. 100, 254105-254108.

Maeki, M., Yamaguchi, H., Tokeshi, M., Miyazaki, M., 2016. Microfluidic approaches for protein crystal structure analysis. Anal. Sci. 32, 3-9.

Maleki, A., Rahimi, R., Maleki, S., Hamidi, N., 2014. Synthesis and characterization of magnetic bromochromate hybrid nanomaterials with triphenylphosphine surface-modified iron oxide nanoparticles and their catalytic application in multicomponent reactions. RSC Adv. 4, 29765-29771.

Mashaghi, S., van Oijen, A.M., 2016. Droplet microfluidics for kinetic studies of viral fusion. Biomicrofluidics 10, 241021-241030.

Mashaghi, S., Abbaspourrad, A., Weitz, D.A., van Oijen, A.M., 2016. Droplet microfluidics: A tool for biology, chemistry and nanotechnology. Trends Anal. Chem. 82, 118-125.

Nguyen, T.Y., Roessler, E.A., Rademann, K., Emmerling, F., 2016. Control of organic polymorph formation: crystallization pathways in acoustically levitated droplets. Cryst. Mater. 232, 15-24.

Okoli, C., Boutonnet, M., Mariey, L., Järås, S., Rajarao, G., 2011. Application of magnetic iron oxide nanoparticles prepared from microemulsions for protein purification. J. Chem. Technol. Biotechnol. 86, 1386-1393.

Phillips, W.T., Lignos, G.I., Maceiczyk, M.R., deMello, J.A., deMello, C.J., 2014. Nanocrystal synthesis in microfluidic reactors: where next? Lab Chip. 14, 3172.

Seemann, R., Brinkmann, M., Pfohl, T., Herminghaus, S., 2012. Droplet based microfluidics. Rep. Prog. Phys. 75, 16601-16643.

Shum, H.C., Abate, A.R., Lee, D., Studart, A.R., Wang, B.G., Chen, C.H., Thiele, J., Shah, R.K., Krummel, A., Weitz, D.A., 2010. Droplet microfluidics for fabrication of non-spherical particles. Macromol. Rapid Commun. 31, 108-118.

Simmons, M., Wiles, C., Rocher, V., Francesconi, M.G., Watts, P., 2013. J. Flow Chem. 3, 7-10.

Song, H., Bringer, M.R., Tice, J.D., Gerdts, C.J., Ismagilov, R.F., 2003. Experimental test of scaling of mixing by chaotic advection in droplets moving through microfluidic channels. Appl. Phys. Lett. 83, 4664-4666.

Song, H., Tice, J.D., Ismagilov, R.F., 2003. A microfluidic system for controlling reaction networks in time. Angew. Chem. Int. Ed. 115, 792-796.

Ushikubo, F.Y., Birribilli, F.S., Oliveira, D.R.B., Cunha, R.L., 2014. Y- and T-junction microfluidic devices: effect of fluids and interface properties and operating conditions. Microfluid Nanofluid. 17, 711-720.

Vitry, Y., Teychene, S., Charton, S., Lamadie, F., Biscans, B., 2015. Investigation of a microfluidic approach to study very high nucleation rates involved in precipitation processes. Chem. Eng. Sci. 133, 54-61.

Wahajuddin, Arora, S., 2012. Superparamagnetic iron oxide nanoparticles: magnetic nanoplatforms as drug carriers. Int. J. Nano. 7, 3445-3471.

Wang, K., Lu, Y.C., Qin, K., Wang, G.S,T., 2013. Generating gas-liquid-liquid three-phase microflows in a cross-junction microchannel device. Chem. Eng. Technol. 36, 1047-1060.

Wang, K., Lu, Y.C., Xu, J.H., Luo, G.S., 2009. Determination of dynamic interfacial tension and its effect on droplet formation in the T-shaped microdispersion process. Langmuir. 25, 2153-2158.

Wang, J.T., Wang, J., Han J.J., 2011. Fabrication of advanced particles and particle-based materials assisted by droplet-based microfluidics. Small. 7, 1728-1754.

Wootton, R.C.R., Demello, A.J., 2012. Microfluidics: analog-to-digital drug screening. Nature. 483, 43-44.

Wu, W., He, Q.G., Jiang, C.Z., 2008. Magnetic iron oxide nanoparticles: synthesis and surface functionalization strategies. Nano. Res. Lett. 3, 397-415.

Wu, Z., Cao, Z., Sundén, B., 2017. Liquid-liquid flow patterns and slug hydrodynamics in square microchannels of cross-shaped junctions. Chem. Eng. Sci. 174, 56-66.

Yagodnitsyna, A.A., Kovalev, V.A., Bilsky, V.A., 2016. Flow patterns of immiscible liquid-liquid flow in a rectangular microchannel with T-junction. Chem. Eng. J. 303, 547-554.

Zhong, L.S., Hu, J.S., Liang, H.P., Cao, A.M., Song, W.G., Wan, L.J., 2006.

Self-assembled 3D flowerlike iron oxide nanostructures and their application in water treatment. Adv. Mater. 18, 2426-2431.

Zhao, Y.C., Chen, G.W., Yuan, Q., 2006. Liquid-liquid two-phase flow patterns in a rectangular microchannel. AIChE J. 52, 4052-4060.

Zhao, Y.C., Chen, G.W., Yuan, Q., 2007. Liquid-liquid two-phase mass transfer in the T-junction microchannels. AIChE J. 53, 3042-3053.

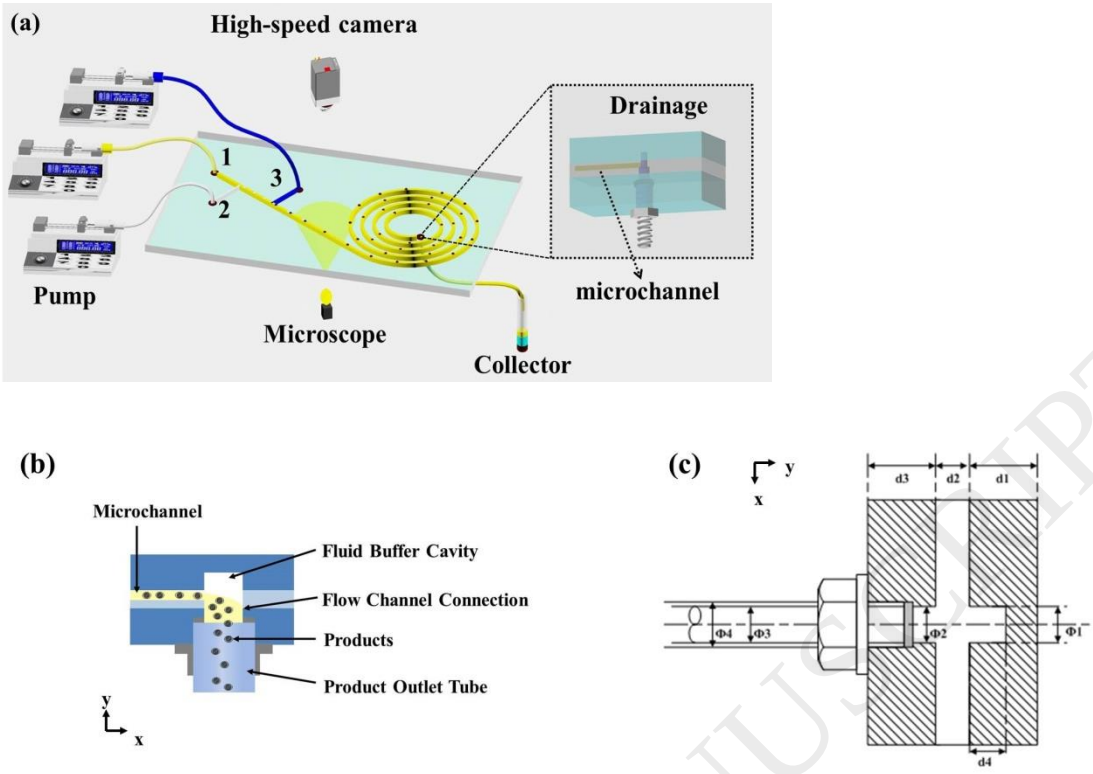

Fig. 1. The schematic diagram of experimental set-up (a) Schematic illustration of the microreactor design and experimental set-up (Inlet 1: oil phase; Inlet 2: OH^- solution; Inlet 3: Fe^{2+}/Fe^{3+} solution), (b) schematic of the anti-clogging structure (a profile of the X-Y direction), and (c) size diagram of the anti-clogging structure

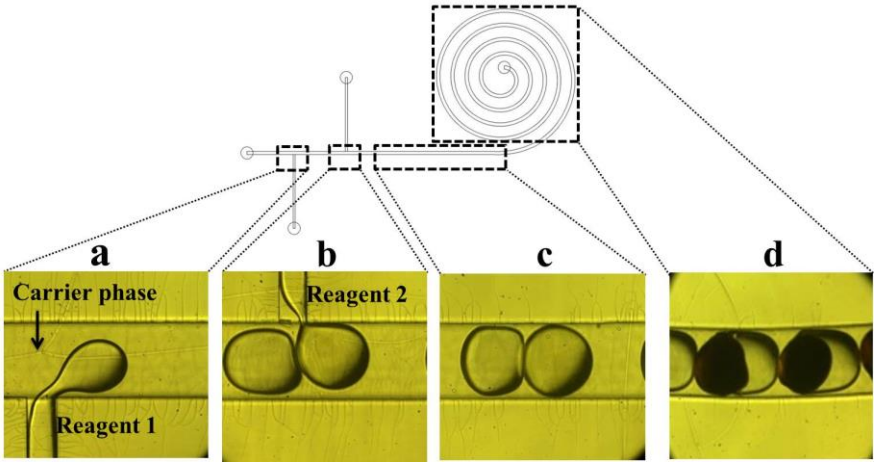

Fig. 2. Four stages of droplets generation and flow with formation of Fe_3O_4 inside the droplets: (a) Droplets dispersion; (b) Droplets collision; (c) Droplets pairing; (d) Droplets fusion with reaction

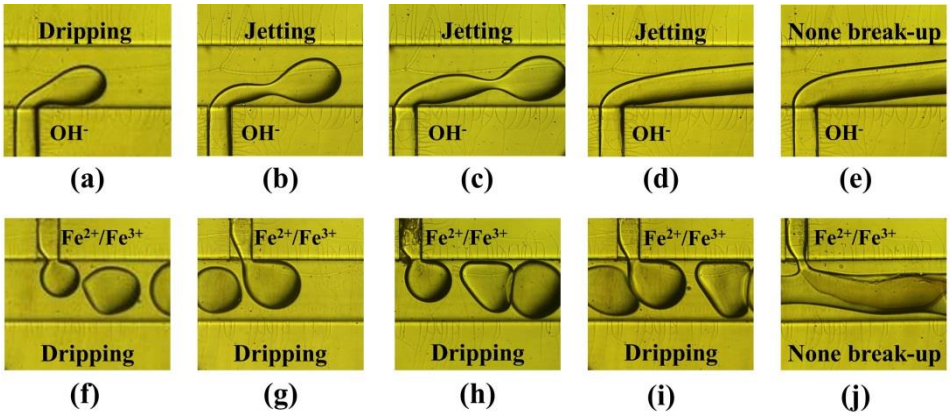

Fig. 3. Droplet generation and typical flow patterns with dispersed solution at varied flow rates Q_D: (a) 5 µL/min, (b) 10 µL/min, (c) 15 µL/min, (d) 20 µL/min, and (e) 40 µL/min. Top: OH^- solution through the first T-junction. Bottom: Fe^{2+}/Fe^{3+} solution through the second T-junction

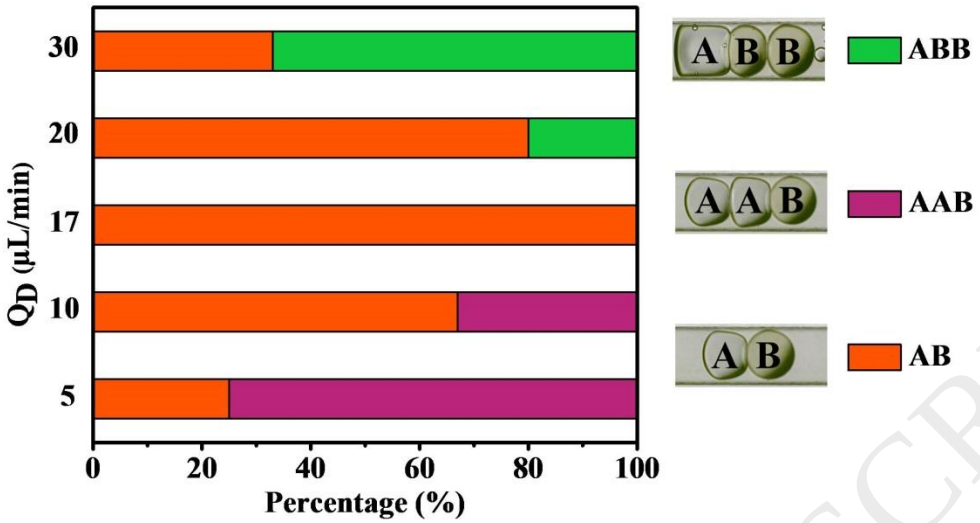

Fig. 4. Pairing modes at different Q_D values, with a fixed Q_C = 40 μL/min

(A: OH^- droplet; B: Fe^{2+}/Fe^{3+} droplet)

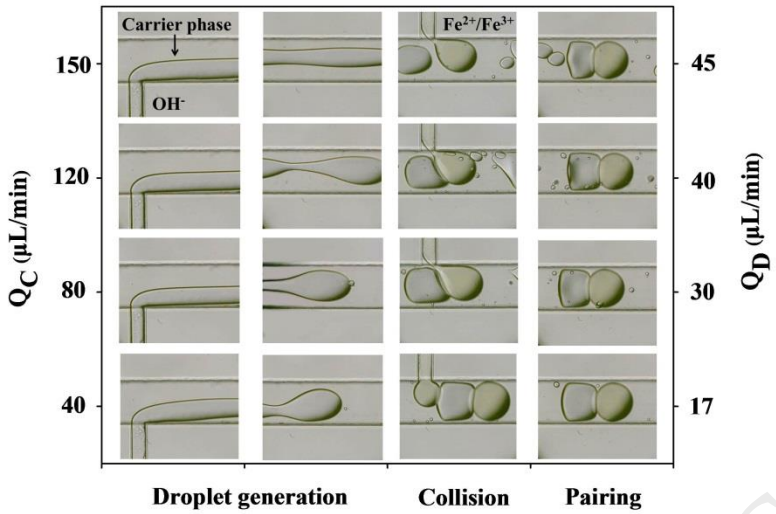

Fig. 5. Flow regimes at different flow rate (The vertical axis represents total flow rate of continuous and dispersed phases, respectively)

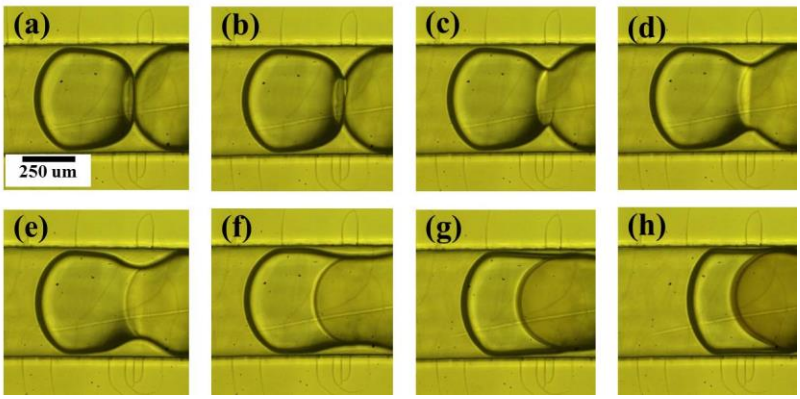

Fig. 6. Interfacial precipitation process of magnetic iron oxide

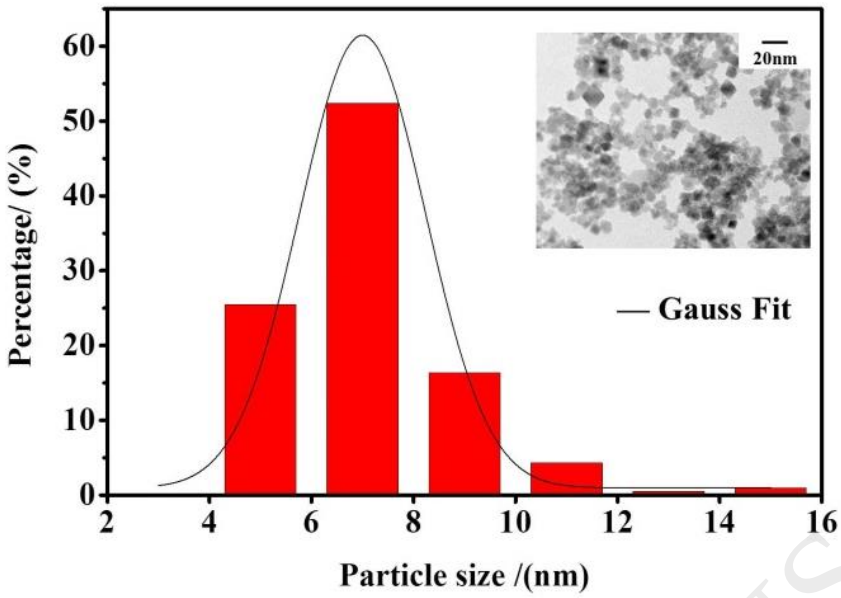

Fig. 7. Particle size distribution and TEM micrograph of Fe_3O_4 nanoparticles synthesized (Q_C = 40 μL/min, Q_D = 17 μL/min)

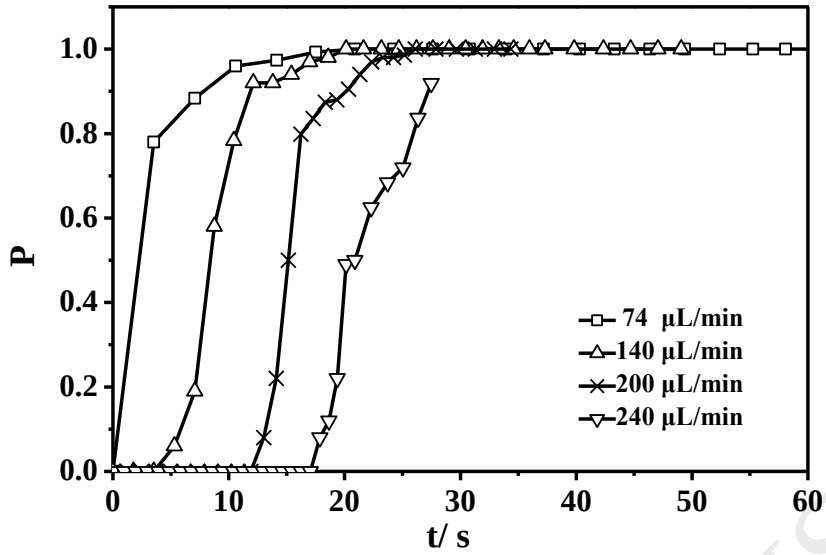

Fig. 8. The temporal evolution of P for four flow rates: (□) 74 μL/min, (Δ) 140 μL/min, (×) 200 μL/min, and (▽) 240 μL/min.

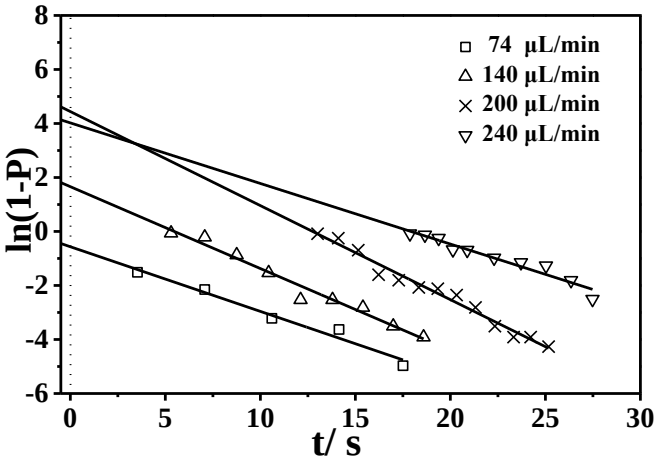

Fig. 9. The relationship between ln (1-P) and time t for different flow rates at (□) 74 μL/min, (Δ) 140 μL/min, (×) 200 μL/min, and (▽) 240 μL/min.

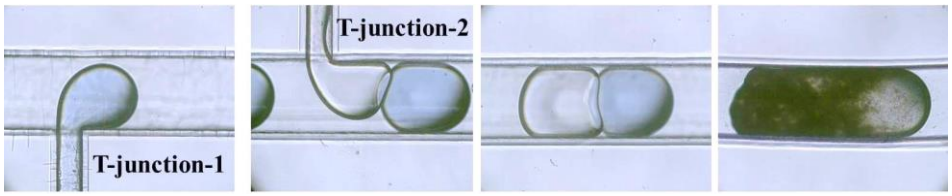

Fig. 10. Four stages of droplets generation and flow with formation of $CaCO_3$ inside the droplets. Where the $CaCl_2$ solution was injected at the T-junction-1 and the Na_2CO_3 solution is injected at the T-junction-2

Table 1. Capillary numbers at different Q_D.

Q_D (μL/min)	Capillary number ($\times 10^{-3}$)	
	Fe^{2+}/Fe^{3+}	OH^-
5	0.0531	0.765
10	0.106	1.53
15	0.159	2.29
20	0.212	3.05
40	0.425	6.11

Table 2. Crystallinity of crystals obtained at different velocities.

Q_C (μL/min)	Q_D (μL/min)	Crystallinity (%)
40	17	38.86
80	30	35.45
120	40	23.67
150	45	22.07

Table 3. Calculated values of the nucleation process at a given flow rate.

Q ($\mu L \cdot min^{-1}$)	V (nL)	ω (s^{-1})	J ($\times 10^{-3}$) ($\mu L^{-1} \cdot s^{-1}$)
74	85	0.24	2.82
140	78	0.30	3.85
200	71	0.35	4.93
240	66	0.22	3.33